SERS Hot Paper

How to cite: *Angew. Chem. Int. Ed.* **2022,** *61,* e202200072
International Edition: doi.org/10.1002/anie.202200072
German Edition: doi.org/10.1002/ange.202200072

Widefield SERS for High-Throughput Nanoparticle Screening

Matz Liebel, Irene Calderon, Nicolas Pazos-Perez, Niek F. van Hulst,* and Ramon A. Alvarez-Puebla**

Abstract: Surface-enhanced Raman scattering (SERS) imaging is a powerful technology with unprecedent potential for ultrasensitive chemical analysis. Point-by-point scanning and often excessively long spectral acquisition-times hamper the broad exploitation of the full analytical potential of SERS. Here, we introduce large-scale SERS particle screening (LSSPS), a multiplexed widefield screening approach to particle characterization, which is 500–1000 times faster than typical confocal Raman implementations. Beyond its higher throughput, LSSPS simultaneously quantifies both the sample's Raman and Rayleigh scattering to directly quantify the fraction of SERS-active particles which allows for an unprecedented correlation of SERS activity with particle size. .

Introduction

Surface-enhanced Raman scattering (SERS) spectroscopy is an ultrasensitive molecular spectroscopy with detection sensitivity down to the single molecule limit.[1] This technique, coupled with a microscope, allows for not only the chemical and structural analysis of two- and three-dimensional biological and non-biological materials, but also the development of optical sensors with sub-micrometer spatial resolution. In fact, SERS microspectroscopy has been successfully used in biological applications[2] for the immunostaining of tissues for cancer diagnosis,[3] phenotypic classification of cells,[4] real-time monitoring of the metabolism in living cells[5] or visualizing drug delivery at the cellular level.[6] SERS imaging has also been widely applied in environmental science,[7] for the characterization of ancient paintings,[8] the engineering of optical sensors[9] and even for the characterization of surfaces[10] and single particles.[11] The real potential of this technique is, however, hindered by its imaging operation. Contrary to other, color-blind, imaging techniques, where images are often acquired in a so-called widefield geometry by simultaneously exciting the entire sample, SERS maps are constructed from many local point- or line-exposures, which are ultimately combined to generate an image. This scanning process is slow and, consequently, suffers from several intrinsic problems. First, even smaller maps are composed of several hundred spectra, with total acquisition times of many minutes or even hours. Quantitative imaging over such extended time-scales is non-trivial. Additionally, this problem is exacerbated in samples where illumination pre-imaging due to, for example, the tails of the illumination spot, may cause irreversible damage via photosublimation, photocombustion, photobleaching and/or photoreaction.[12] Second, considering the high spatial resolution of the maps, with step sizes of 1 μm^2 and below, even minor mechanical instabilities, over the often minutes-to-hours long acquisition periods, may translate into SERS map artifacts. In summary, there is a need for innovative approaches that enable fast SERS interrogation of both single particles and aggregates. Such approaches would enable much needed quantitative SERS-sample characterization as well as their application in sensing schemes in the context of tissues, cells or other surfaces.[13]

Here, we present large-scale SERS particle screening (LSSPS) which allows acquiring spectra of many thousands of individual SERS particles. LSSPS is based on a simple-to-implement highly multiplexed widefield optical microscope[14] capable of generating single-shot SERS maps of many individual particles within seconds. Beyond these capabilities, our microscope simultaneously quantifies the sample's Rayleigh scattering, thus allowing for an unprecedented classification of plasmonic materials by correlating SERS activity with the particle-size dependent scattering intensity. To demonstrate the working principles and high throughput of this screening platform, we prepared several types of SERS nanoparticles (NPs), which we labeled, or encoded, with different types of molecules, and with a large

[*] Dr. M. Liebel, Prof. Dr. N. F. van Hulst
ICFO - Institut de Ciencies Fotoniques,
The Barcelona Institute of Science and Technology,
Castelldefels, Barcelona (Spain)
E-mail: matz.liebel@icfo.eu
niek.vanhulst@icfo.eu

I. Calderon, Dr. N. Pazos-Perez, Prof. Dr. R. A. Alvarez-Puebla
Department of Physical and Inorganic Chemistry and EMaS,
Universitat Rovira i Virgili
Tarragona (Spain)
E-mail: ramon.alvarez@urv.cat

Prof. Dr. N. F. van Hulst, Prof. Dr. R. A. Alvarez-Puebla
ICREA - Institució Catalana de Recerca i Estudis Avançats,
Barcelona (Spain)

enough optical efficiency to allow facile single-NP observations.

Results and Discussion

Figure 1 explains our SERS-particle synthesis strategy and shows TEM images of the SERS encoded NP-aggregates[15] which we will refer to as core@satellite structures throughout the manuscript. Briefly, 15 nm diameter silver NPs (i.e., satellites, Figure 1b) were produced following a previously reported protocol.[16] Silver NPs with 90 nm diameter were prepared via kinetically controlled growth[17] (i.e., cores, Figure 1b) using citrate and ascorbate as both surfactants and reducing agent. Both NPs were then encoded with the SERS reporters by first coating them with mercaptoundecanoic acid (MUA) followed by addition of the molecular labels, or SERS codes.

These codes diffuse into the aliphatic pockets created by the MUA and bind to the metallic surface without perturbing the colloidal stability of the particles, regardless of the chemical nature of the molecular reporter.[18] Due to the alkaline environment, the acidic terminal group of MUA was ionized resulting in a NP surface charge (i.e. zeta potential) of −46 and −52 mV for NPs of 90 and 15 nm, respectively. Thus, to form the core@satellite structures, the cores were coated with a submonolayer of polyethylenimine (PEI), under well-controlled conditions, until the zeta potential reached 35 mV. This suspension of positively charged cores was then added dropwise to a solution containing the negatively charged satellites. Following electrostatic retention of the satellites onto the cores, the resulting sols were extensively cleaned to remove the remaining free satellites. The core@satellite assembly was then coated with silica (Figure 1b) to ensure optical and colloidal stability. Optical characterization via localized surface plasmon resonance (LSPR) measurements shows the characteristic bands at 390 nm and 482 nm for the single Ag NPs of 15 nm and 90 nm, respectively (Figure 1c). The

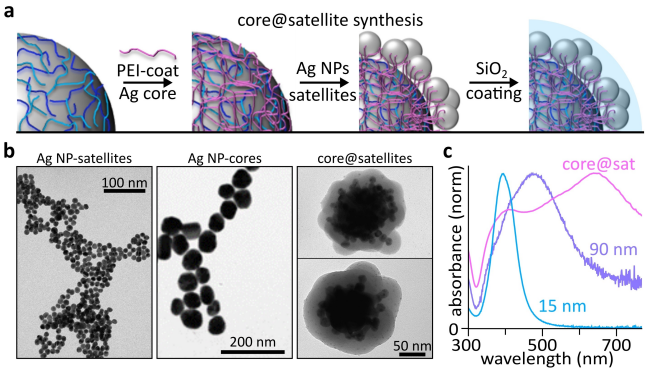

Figure 1. a) Illustrative description of the fabrication of silver core@satellite SERS encoded nanoparticles. b) TEM images of the satellites (AgNPs, 15 nm, left), cores (AgNPs, 90 nm, centre) and high-resolution TEM images of the core@satellites coated with silica (right). c) Normalized localized surface plasmon resonances for the satellites, cores and their assemblies.

core@satellite complexes exhibit a notable redshift to 658 nm due to hot-spot formation[19] between both the core and the satellites as well as between individual satellites.[20]

Figure 2 presents characterizations of the five different SERS codes employed in this study: rhodamine 6G, R6G; 3,4-dichlorobenzenethiol, DCBT; 4-fluorobenzenethiol, FBT; 4′-bromo-4-mercaptobiphenyl, BMBP; and, 4-(dimethylamino)benzenethiol, DMBT. We spin-coated particles onto #1.5 microscope cover slides, achieving approximate particle densities 0.02 particles per μm^2. To ensure the presence of single core@satellite assemblies, rather than large aggregates, we first SEM visualized the structures (Figure 2a).[21] Figure 2b shows representative SERS maps obtained with a confocal Raman microscope in the typical point-by-point scanning mode. The mapped area (21 × 21 μm) is composed of 441 spectra that were acquired with an integration time of 1 s per point. Obtaining the full image hypercube thus required approximately 8 mins of pure observation time. We note, however, that we are considerably under sampling as the nominal pixel size of 1 μm is larger than the diffraction limit of 420 nm: imaging at the Nyquist limit would have required a total of 42 mins of observation time. Irrespective, the SERS spectra of individual clusters in combination with the SEM images (Figure 2a–c) confirm the successful synthesis and functionalization of the five SERS codes. The rather slow conventional imaging throughput, however, severely hampers our ability to perform systematic sample characterizations on large numbers of individual SERS particles, a limitation that ultimately prevents powerful diagnostics and sensing applications based on large-scale single-particle imaging.

The LSSPS platform solves the aforementioned visualization challenge and enables high-speed imaging of large numbers of individual SERS codes in a fully automated fashion (Figure 3). Rather than point-scanning across the sample we widefield-illuminated a 120 μm diameter sample-area and collected the generated Raman scattering with a diffraction limited spatial resolution of approximately 240 nm. The collected light propagated through a custom-build "imaging and spectroscopy" module that simultaneously acquired so-called reference and spectral images on the same sCMOS camera (Supporting Information). The reference image, containing approximately 10 % of all collected photons, reports on the particles' positions in the sample plane albeit in a color-blind fashion. The information content is hence comparable to the integrated confocal SERS maps shown in Figure 2b. In the spectral channel, we spectrally dispersed the image by inserting a prism into the relay imaging system as shown in Figure 3. The combination of the position and the spectral channel ultimately allows extracting single-particle spectra from the widefield recording (Supporting Information) as the particles' positions define their respective wavenumber axis. We further used a flat illumination profile to ensure quantitative signal magnitudes (Supporting Information). Ultimately, we imaged the exact same samples as already used in the experiments presented in Figure 2. Rather than raster-scanning a 1 μm confocal spot, however, we scanned a 120 μm illumination area across the sample thus giving us a nominal $>10^4$-fold

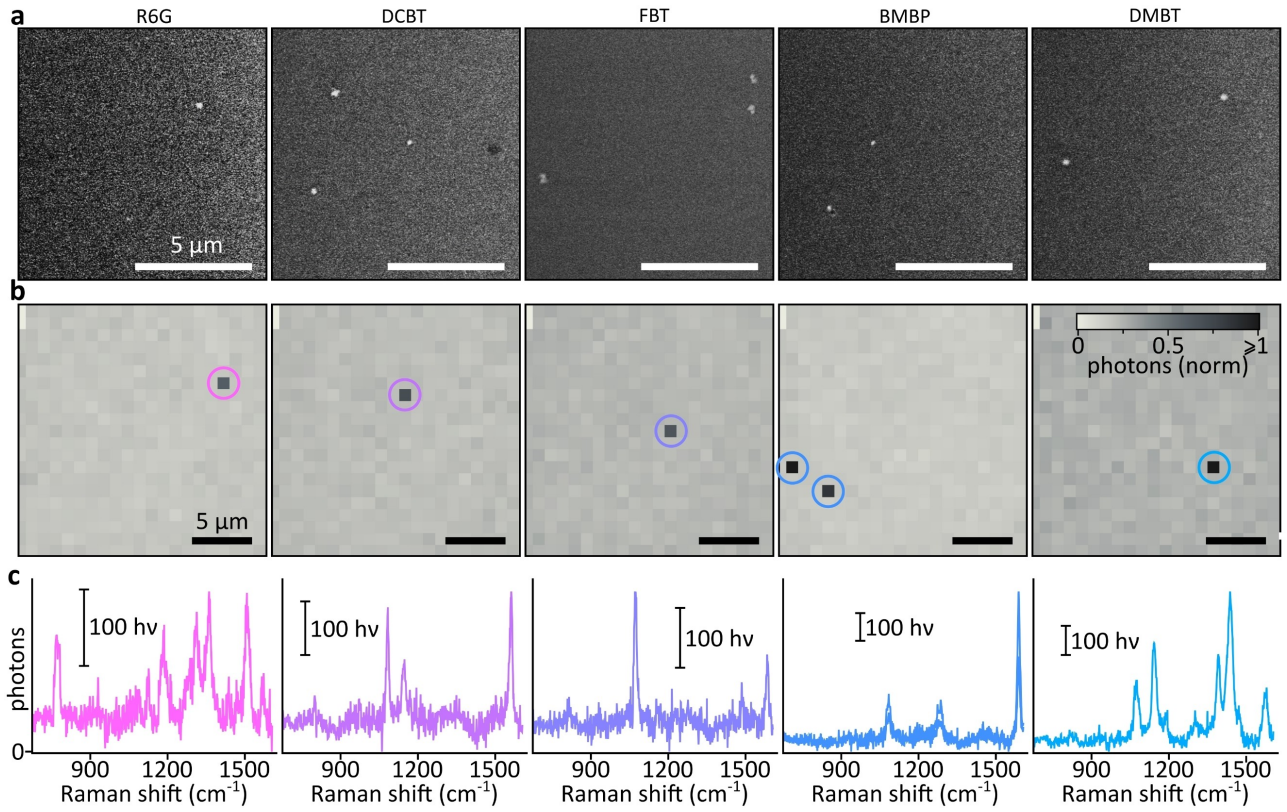

Figure 2. a) SEM images for core@satellites encoded particles labelled with five different SERS codes (rhodamine 6G, R6G; 3,4-dichlorobenzenethiol, DCBT; 4-fluorobenzenethiol, FBT; 4′-bromo-4-mercaptobiphenyl, BMBP; and, 4-(dimethylamino)benzenethiol, DMBT). b) SERS maps and c) SERS spectra of the particles obtained with a confocal Raman microscope using a 633 nm laser line and a 50×0.75 NA objective at an excitation fluence of 160 W cm^{-2}. The size of the map (21×21 µm) is composed of 441 spectra that required ≈8 min of observation time (integration time of 1 s pixel^{-1}). All SERS images are plotted using the same xy-scale and photon-range, higher photon numbers are capped for representation purposes, as indicated in the scale-bar.

throughput advantage and a total observation area of several mm^2, depending on the total number of images acquired.

Figure 4a shows representative, median-background subtracted (Supporting Information), sample images (top) and spectrally dispersed images (bottom) for the 5 different SERS codes acquired on the same samples as previously used in Figure 2. These images were obtained with a 60× objective and a grating-filtered 638 nm diode laser (Supporting Information), with a fluence of 270 W cm^{-2}. Each image was obtained by averaging 10 acquisitions with an exposure time of 200 ms per image (total measurement time of 2 s) while flat-top illuminating the sample. As explained previously, the position information of the individual particles allows isolating their spectra from the dispersed channel[14] to, ultimately, extract the SERS spectra of all individual particles (Figure 4a, b).

Even the few spectra shown in Figure 4b already highlight distinct differences between individual particles in terms of background luminescence, SERS intensities and ratios of the individual Raman active modes. More importantly, LSSPS relies on autonomous image-acquisition thus allowing us to characterize thousands of individual SERS codes. Figure 5a highlights these capabilities, showing the amplitude-sorted spectra of 3809 DCBT-labeled core@satellites obtained from a total of 775 images, on a total area of ≈10 mm^2, of the extremely sparse sample described above, containing only ≈5 SERS-active particles per 120x120 µm^2 field-of-view.

Figure 5b presents representative single-particle spectra for both dim (top two) and bright (bottom two) particles, highlighting strong inter-particle differences. For example, the bright spectra exhibit near-identical integrated photon counts but their Raman spectrum-to-background ratios differ dramatically. One spectrum is background-dominated with very weak Raman signatures while the other shows strong SERS activity with little luminescence-background contributions.

To further explore how ensemble spectra compare to single-particle observations we repeated the experiment outline above and acquired 775 images for each of the five SERS codes. Even though we used samples with nominally identical particle densities we obtained "only" 1500 to as many as 11 000 single-particle spectra, depending on the SERS code. This difference might be due to non-uniform spin-coating, particle aggregation post-synthesis, contamination of the core@satellites with single particles and plain silica spheres (see Figure S1), or code-specific functionaliza-

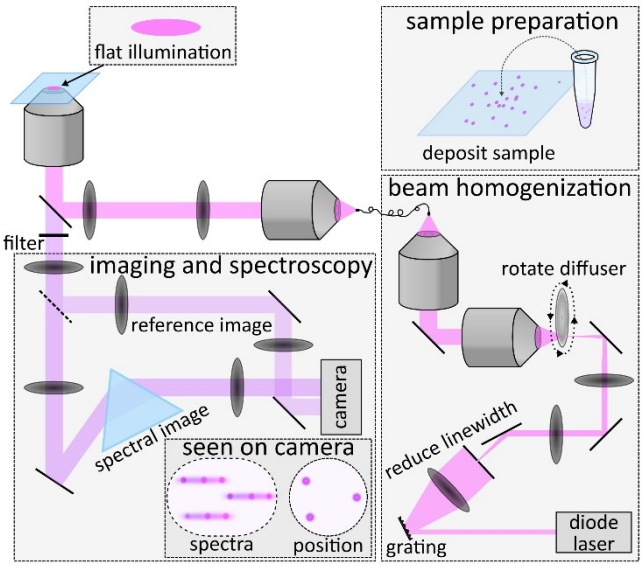

Figure 3. Schematic of the LSSPS platform composed of a standard widefield microscope extended with "beam homogenization" and "imaging and spectroscopy" modules. The beam homogenization module (Supporting Information) ensures a flat illumination profile over the entire field of observation to allow quantitative SERS intensity measurements. The imaging and spectroscopy unit simultaneously records an image of the sample plane alongside a spectrally dispersed copy of said image on the same sCMOS camera (Supporting Information). This combination ultimately allows extracting single-particle spectra from the camera recordings (Supporting Information).

tion-success and brightness. The mean spectra, estimated based on particles exhibiting moderate intensities (40–60 % fraction), show good spectral agreement with ensemble-based Raman spectra (Figure 5c) but also highlight interesting SERS-to-background differences between the codes. These variations can be ascribed to geometrical effects and surface selection rules[22] which ultimately alter the Raman activity of the different vibrational modes of the coding molecules due to the monolayer packing in the metallic surface, which might result in an overall reduction of all SERS bands in the mean spectrum. In fact, this is a common observation in single-molecule SERS spectra of anisotropic nanoparticles or aggregates, regardless of their homogeneity.

To gain further insight we performed some basic statistical analysis (Figure 5d), comparing single-particle luminescence backgrounds (evaluated in the spectrally silent 875–950 cm^{-1} region), maximum emission intensities and signal-to-background levels. The latter attempts isolating the pure SERS contribution by removing the luminescence background counts. Even though considerable differences are present between all distribution functions the variability is considerably reduced in the background-subtracted fraction. In our logarithmic basis, these functions are reminiscent of normal distributions centred around 300–400 photons albeit at varying variances and some outliers towards very high/low photon counts. In other words, even though the ensemble spectra (Figure 5c) indicated that DCBT might be poorly performing the single-particle analysis (Figure 5b,d) revealed that a large sub-ensemble with satisfactory SERS-brightness existed. The most likely reason for the low mean-signal is the presence of residual single Ag-particles and plain silica spheres.

To highlight the importance of characterizing such variability, a task difficult to achieve with conventional microscopes due to their limited throughput, we now focus on the FBT code. Figure 6a shows an amplitude map composed of 5134 FBT-labelled core@satellite single particle spectra. Contrary to our previous analysis which relied on total photon-emission (Figure 5a), we now sorted the spectra based on a ratio of maximum counts to mean background signal. The rationale behind this choice is to distinguish highly SERS-active from inactive particles, such as bare Ag or condensed silica NPs. Indeed, principal component analysis (PCA) performed on the top (bottom) ten percent of these sorted spectra allowed extracting representative "SERS" and "luminescence" spectra as the first principal component (Figure 6a).

The principal components were then normalized with respect to their mean background level (875–950 cm^{-1} region) and used to classify the entire, equally normalized, dataset. Within the scope of this first implementation of LSSPS we relied on a simple correlation-based classifier without performing the generally necessary validation steps: when the correlation (r) between the measured spectrum and either "SERS" or "luminescence" >0.7 the spectrum is classified accordingly. In all other instances (e.g., $r_{SERS}>0.7$ and $r_{luminescene}>0.7$ or $r_{SERS}<0.7$ and $r_{luminescene}<0.7$) we classify the particle as unknown. Figure 6b shows the resulting classification. 48 % of the particles show very consistent spectral features corelated with "SERS", 25 % show little SERS-activity and the remainder shows dissimilar vibrational patterns to what we expected. Interestingly, even these unknown spectra exhibit highly-conserved features. Based on this classification we computed the mean spectra of the "SERS" and "unknown" fraction and compared it to the sample mean over all particles. This comparison highlights that even though ensemble SERS measurements are highly useful they might only be partially suitable for describing the system (Figure 6c).

Following the approach outlined above we moved on to extract principal component luminescence and SERS spectra for all five codes. We then used these components to attempt correctly classifying the individual SERS codes after combining all spectral measurements. This analysis mimics a potential sensing-scenario where several SERS codes are simultaneously used for multiplexed detection of multiple analytes. As previously, we relied on a simple correlation: if $r>0.7$ for only one principle component spectrum, the particle was assigned to this class; if $r_{luminescene}>0.7$ for multiple luminescence components but $r_{SERS}<0.7$ for all SERS components the particle was assigned to luminescence; if $r<0.7$ for all we assigned the particle to unknown; finally, if $r>0.7$ for more than one component including SERS components we increased the threshold to $r>0.9$ and re-evaluated following the logic outlined above. Figure 6d summarizes the classification results.

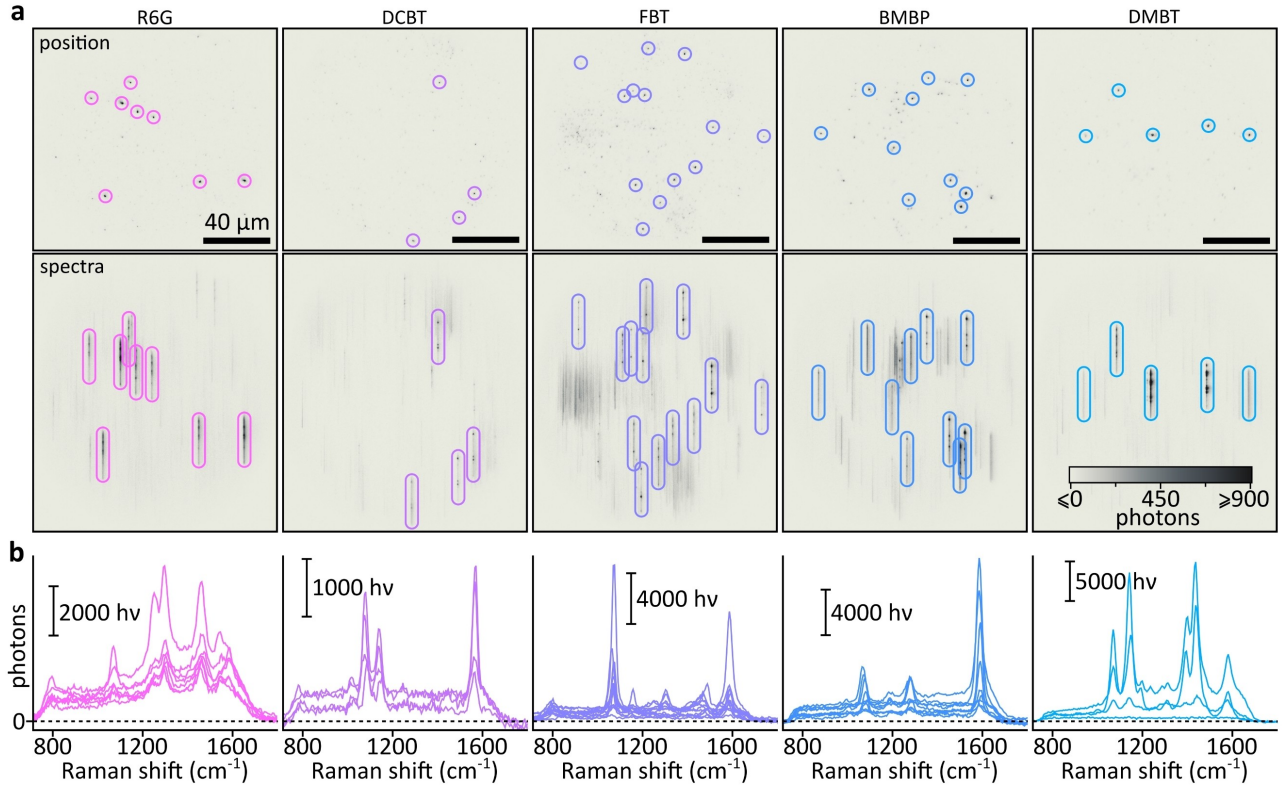

Figure 4. a) Median-background subtracted sample images (top) and spectrally dispersed images (bottom) acquired by LSSPS. Representative, by-hand selected, particles are indicated by circles and their corresponding dispersed images by circular boxes. All images are plotted using the same xy-scale and photon-range, higher/lower photon numbers are capped for representation purposes, as indicated in the scale-bar. Particle-spectra that considerably overlap with other particles were excluded from the selection. b) Raman spectra extracted by integrating the individual particle spectra highlighted in (a).

Based on the previous analysis of the single particle spectra (Figure 6a–c) it is unsurprising that a considerable fraction of the particles, approximately 50 %, is classified as either SERS inactive or unknown, a finding that mainly reflects the difficulties associated with synthesizing highly uniform particles. From an analytical point of view, however, the main concern is regarding false positives, that is incorrectly assigning one SERS code to another SERS class. The table shown in Figure 6d shows that our simple classifier model is ill-suited for classification when the R6G code is included in the analysis which results in considerable misclassification of up to 16 %. However, simply eliminating the R6G code allows restoring near-perfect classification with classification errors <0.5 % for all SERS codes albeit the rather simple algorithm. We anticipate that more advanced feature-selection and classification approaches will enable confident identification of essentially all SERS active codes.

Thus far, we have uncovered discrepancies between ensemble and ensemble-level[23] single particle observations: changes in spectral amplitudes, signal-to-background variations as well as spectral changes reminiscent of chemical or conformational variability on the molecular level. All of these observations crucially relied on detecting frequency-shifted particle luminescence. This approach is ill-suited for quantitatively characterising the SERS code population as it potentially only captures a fraction of the synthesized particles. Non-luminescent particles remain undetected and it is hence difficult to judge the absolute quality of the as-prepared SERS codes. To address this shortcoming, we slightly modified the experimental setup (Figure 3). We moved the laser-rejection filter past the beam-splitter separating the reference and spectral channels and placed a darkfield mask into the conjugate back-focal-plane of the "reference image" channel (Supporting Information). This modification allowed us to darkfield-detect the particles and simultaneously characterize their luminescence properties via the "spectral channel".

Figure 7a shows a representative darkfield image of the spin coated DMBT codes, the sample that showed the smallest number of luminescent particles (Figure 5d). The acquisition of 775 images yields a total of 6760 spectra of different assemblies (Figure 7b) which are classified as either SERS (top) or inactive (bottom), following the previously described PCA protocol. We detected a total of 1848 luminescent particles which is in good agreement with the number of particles observed during the initial experiments (Figure 5c).

Finally, we compared scattering intensities and SERS activity. In routine practice, it is necessary to SEM-characterise the sample, a destructive methodology, and then perform optical measurements on a different subset of

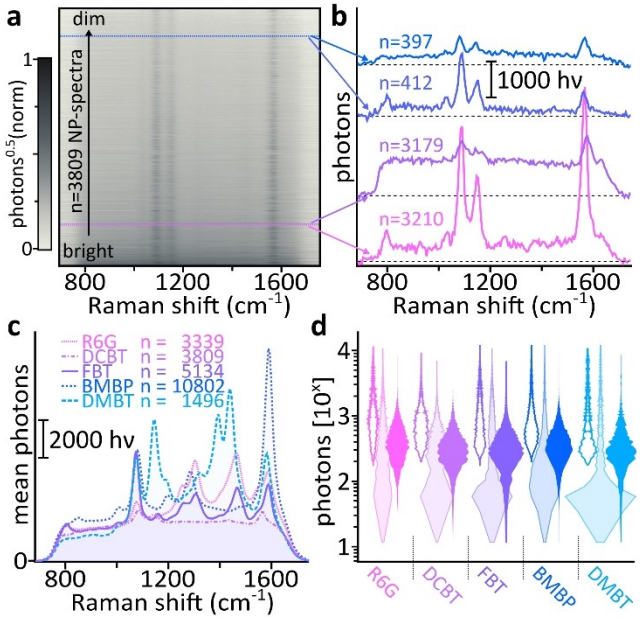

Figure 5. a) Amplitude plot of 3809 single particle spectra recorded for DCBT. The spectra are sorted by their integrated brightness. Square-root intensities (amplitudes) are shown for representation purposes. b) Representative single particle spectra for both dim (top two) and bright (bottom two) candidates. The spectra are offset for clarity, the dashed lines indicate zero photons after median-image subtraction. c) Mean spectra of the five SERS codes, computed based on particles exhibiting moderate brightness (40–60% fraction of the integrated intensity distribution function). d) Emission intensity distribution functions for both background and SERS-signals, calculated based on all single-particle spectra. Unfilled: mean of the 15 largest intensity values; Filled and transparent: mean of the 15 values comprising the background region (875–950 cm^{-1}); Filled: mean of the 15 largest intensity values after background subtraction.

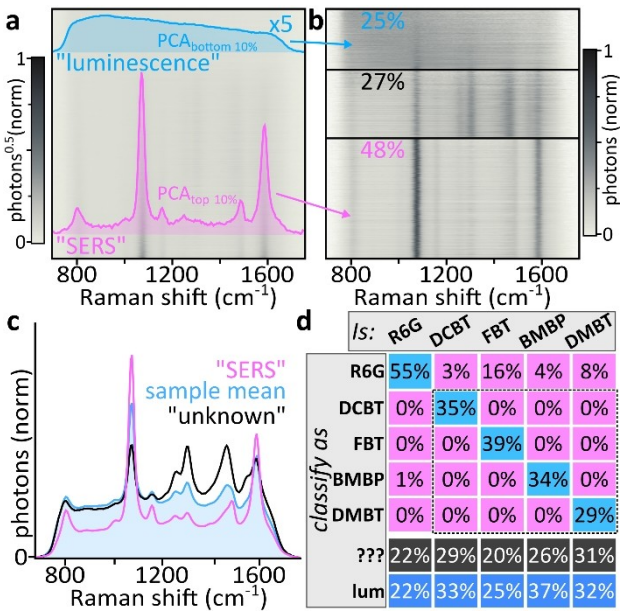

Figure 6. a) Amplitude plot of 5134 FBT-coded single particle spectra sorted by the ratio between maximum value and mean background (875–950 cm^{-1} region). The blue/pink insets show the first principal component obtained by relying on the top (bottom) 10% of the sorted spectra. The fractional variance of the first principal components is 96% ("luminescence") and 87% ("SERS"). b) Classified spectra. Each spectrum is normalised to the mean of its 15 largest values. c) Mean spectra obtained by averaging the normalised "SERS" (pink), non-classified (black) and all (blue, filled) spectra. d) Particle classification based on simple correlation coefficients using the "luminescence" and "SERS" spectra of all 5 types of SERS coded particles, obtained analogous to the FBT example discussed in detail. Each column shows the respective assignment of a measured particle, *???* indicates unknown spectra and *lum* luminescence.

the sample (Figure 2).[21] Albeit yielding valuable insight, the intrinsically low throughput of both techniques makes it difficult to perform statistically sound sample-characterizations. Our approach allows label-free identifying all particles in a non-destructive fashion while simultaneously detecting the luminescence of the same particles. Figure 7c correlates the scattering and luminescence intensities of both the SERS-active and inactive fractions. If we assume that scattering intensity reports on the particle size,[24] then the data suggests that luminescence is largely unaffected by the size. Only the smallest particles seem to exhibit considerably reduced luminescence probabilities, as can be seen by comparing the two scattering intensity probability densities where the inactive fraction exhibits a maximum at the low intensity side. We speculated that these weakly-scattering objects might be only partially assembled particles and hence attempted increasing the percentage of SERS active particles via scattering-intensity based thresholding (Figure 7d). Even though we were able to slightly increase the fraction of active particles, by approximately 7–8%, the overall change is rather small given that we were forced to reject >50% of all detected particles. In other words, SERS activity and particle size seem to, indeed, be relatively uncorrelated, as already seen in Figure 7c. Based on these observations we estimated the fraction of SERS active particles to being 30–35%.

Conclusion

To summarize, we introduced large-scale SERS particle screening (LSSPS): a much-needed approach to SERS imaging and spectroscopy that offers key advantages over conventional confocal Raman microscopy. We implemented the LSSPS platform based on a multiplexed and spectrally dispersed widefield microscope with flat-top illumination to ensure quantitative signal levels over the entire, 120 µm diameter, field of single-shot observation with commonly imaged areas exceeding several mm^2. This approach is theoretically about 10000 times faster than our currently available confocal implementation even though experimental constraints based on particle densities reduces this best-case-scenario to approximately 500–1000 times for realistic particle densities. This increase in acquisition rate is paramount for essentially all SERS imaging applications, but especially for those related to biological samples, including tissues and cells, where photodegradation of the sample or

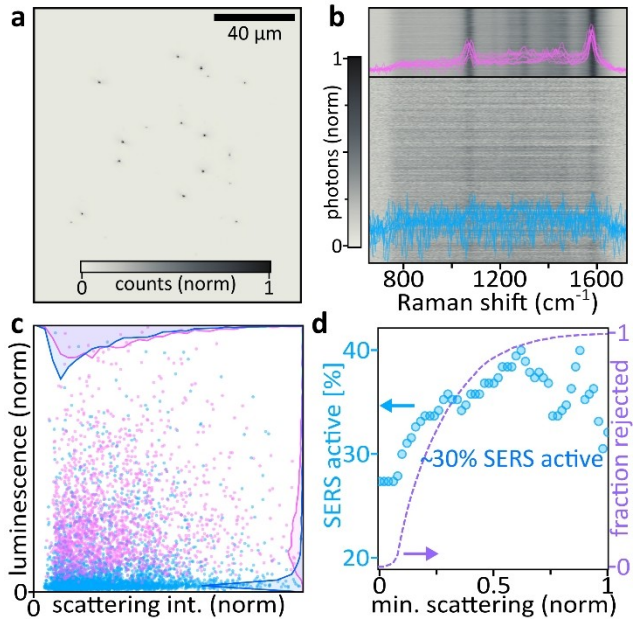

Figure 7. a) Representative darkfield image of the DMBT sample, the normalised counts are capped at 33 % of the image-maximum for representation purposes. b) Spectra of all 6760 particles after classification into SERS-active (top) and inactive (bottom). Each individual spectrum is normalised to the mean of its 15 largest values. The apparent spectral signatures in the inactive fraction are an image pixelation-based representation artefact due to very few unclassified candidates with minor SERS activity. The spectral insets (pink and blue) show 10 consecutive spectra to highlight that most inactive-classified particles indeed show no SERS activity. c) Luminescence and scattering intensity correlation plots alongside probability density functions for the inactive (blue) and SERS-active (pink) fractions. d) Scattering intensity-based thresholding slightly increases the fraction of SERS active particles which is approximately 30–35 %.

photodamage of the biological structure is a severe problem. Importantly, LSSPS allows rapidly collecting thousands of spectra of individual SERS particles, which enables real-time optical characterisation, and potentially feedback-loop based synthesis optimisation, in an unbiased fashion. Beyond the LSSPS methodology, the simultaneous acquisition of widefield images ensures unbiased sample observations by capturing both Raman as well as Rayleigh scattering. Ultimately, these capabilities drastically reduce the need for thorough SEM characterization as Rayleigh scattering directly reports on the sample quality as well as the size of the objects under study. We anticipate that this new family of microscopies will have a deep impact on both the preparation of plasmonic materials and SERS sensors as well as the imaging and analysis of complex samples.

Acknowledgements

M.L. and N.F.v.H. acknowledge support by the Ministry of Science, Innovation, and Universities (MCIU: RTI2018-099957-J-I00 and PGC2018-096875-B-I00). N.F.v.H. acknowledges the financial support by the European Commission (ERC Advanced Grant 670949-LightNet) and the Catalan AGAUR (2017SGR1369). This work was partially funded by CEX2019-000910-S [MCIN/ AEI/10.13039/ 501100011033], Fundació Privada Cellex, Fundació Privada Mir-Puig, and Generalitat de Catalunya through the CERCA program. I.C, N.P.P. and R.A.A.P. acknowledge support by the Ministry of Science, Innovation, and Universities/ AEI (PID2020-120306RB-I00), Ministry of Science, Innovation, and Universities/ European Union Next Generation/ PRTR (PDC2021-121787-I00), the Catalan AGAUR (2017SGR883), and the Universitat Rovira i Virgili (2021PFR-URV-B2-02).

Conflict of Interest

The authors declare no conflict of interest.

Data Availability Statement

The data that support the findings of this study are available from the corresponding author upon reasonable request.

Keywords: Imaging · Nanoparticles · SERS · Widefield Microscopy

[1] a) S. Schlücker, *Angew. Chem. Int. Ed.* **2014**, *53*, 4756–4795; *Angew. Chem.* **2014**, *126*, 4852–4894; b) J. Langer, D. J. de Aberasturi, J. Aizpurua, R. A. Alvarez-Puebla, B. Auguié, J. J. Baumberg, G. C. Bazan, S. E. J. Bell, A. Boisen, A. G. Brolo, J. Choo, D. Cialla-May, V. Deckert, L. Fabris, K. Faulds, F. Javier García de Abajo, R. Goodacre, D. Graham, A. J. Haes, C. L. Haynes, C. Huck, T. Itoh, M. Käll, J. Kneipp, N. A. Kotov, H. Kuang, E. C. Le Ru, H. K. Lee, J. F. Li, X. Y. Ling, S. A. Maier, T. Mayerhöfer, M. Moskovits, K. Murakoshi, J. M. Nam, S. Nie, Y. Ozaki, I. Pastoriza-Santos, J. Perez-Juste, J. Popp, A. Pucci, S. Reich, B. Ren, G. C. Schatz, T. Shegai, S. Schlücker, L. L. Tay, K. George Thomas, Z. Q. Tian, R. P. van Duyne, T. Vo-Dinh, Y. Wang, K. A. Willets, C. Xu, H. Xu, Y. Xu, Y. S. Yamamoto, B. Zhao, L. M. Liz-Marzán, *ACS Nano* **2020**, *14*, 28–117; c) M. Fan, G. F. S. Andrade, A. G. Brolo, *Anal. Chim. Acta* **2020**, *1097*, 1–29.
[2] A. G. Brolo, *Nat. Photonics* **2012**, *6*, 709–713.
[3] a) X. Qian, X.-H. Peng, D. O. Ansari, Q. Yin-Goen, G. Z. Chen, D. M. Shin, L. Yang, A. N. Young, M. D. Wang, S. Nie, *Nat. Biotechnol.* **2008**, *26*, 83–90; b) Q. Li, X. Ge, J. Ye, Z. Li, L. Su, Y. Wu, H. Yang, J. Song, *Angew. Chem. Int. Ed.* **2021**, *60*, 7323–7332; *Angew. Chem.* **2021**, *133*, 7399–7408.
[4] D. Jimenez de Aberasturi, A. B. Serrano-Montes, J. Langer, M. Henriksen-Lacey, W. J. Parak, L. M. Liz-Marzán, *Chem. Mater.* **2016**, *28*, 6779–6790.
[5] a) P. Riveragil, C. Vazquez-Vazquez, V. Giannini, M. P. Callao, W. J. Parak, M. A. Correa-Duarte, R. A. Alvarez-Puebla, *Angew. Chem. Int. Ed.* **2013**, *52*, 13694–13698; *Angew. Chem.* **2013**, *125*, 13939–13943; b) K. P. Valente, A. Suleman, A. G. Brolo, *ACS Appl. Bio Mater.* **2020**, *3*, 6992–7002; c) Z. Zhang, X. Han, Z. Wang, Z. Yang, W. Zhang, J. Li, H. Yang, X. Y. Ling, B. Xing, *Chem. Commun.* **2018**, *54*, 7022–7025.
[6] C. Carrillo-Carrión, R. Martínez, M. F. Navarro Poupard, B. Pelaz, E. Polo, A. Arenas-Vivo, A. Olgiati, P. Taboada, M. G. Soliman, Ú. Catalán, S. Fernández-Castillejo, R. Solà, W. J.

Parak, P. Horcajada, R. A. Alvarez-Puebla, P. del Pino, *Angew. Chem. Int. Ed.* **2019**, *58*, 7078–7082; *Angew. Chem.* **2019**, *131*, 7152–7156.
[7] R. A. Álvarez-Puebla, L. M. Liz-Marzán, *Energy Environ. Sci.* **2010**, *3*, 1011–1017.
[8] A. Cesaratto, M. Leona, J. R. Lombardi, D. Comelli, A. Nevin, P. Londero, *Angew. Chem. Int. Ed.* **2014**, *53*, 14373–14377; *Angew. Chem.* **2014**, *126*, 14601–14605.
[9] a) J. J. S. Rickard, V. Di-Pietro, D. J. Smith, D. J. Davies, A. Belli, P. G. Oppenheimer, *Nat. Biomed. Eng.* **2020**, *4*, 610–623; b) L. Guerrini, E. Garcia-Rico, N. Pazos-Perez, R. A. Alvarez-Puebla, *ACS Nano* **2017**, *11*, 5217–5222; c) Z. Liu, J. Ai, P. Kumar, E. You, X. Zhou, X. Liu, Z. Tian, P. Bouř, Y. Duan, L. Han, N. A. Kotov, S. Ding, S. Che, *Angew. Chem. Int. Ed.* **2020**, *59*, 15226–15231; *Angew. Chem.* **2020**, *132*, 15338–15343; d) A. Qu, M. Sun, L. Xu, C. Hao, X. Wu, C. Xu, N. A. Kotov, H. Kuang, *Proc. Natl. Acad. Sci. USA* **2019**, *116*, 3391–3400.
[10] Y. Liu, Y. H. Lee, M. R. Lee, Y. Yang, X. Y. Ling, *ACS Photonics* **2017**, *4*, 2529–2536.
[11] a) L. Rodríguez-Lorenzo, R. A. Álvarez-Puebla, I. Pastoriza-Santos, S. Mazzucco, O. Stéphan, M. Kociak, L. M. Liz-Marzán, F. J. G. De Abajo, *J. Am. Chem. Soc.* **2009**, *131*, 4616–4618; b) M. Caldarola, P. Albella, E. Cortés, M. Rahmani, T. Roschuk, G. Grinblat, R. F. Oulton, A. V. Bragas, S. A. Maier, *Nat. Commun.* **2015**, *6*, 7915; c) C. S. L. Koh, H. K. Lee, G. C. Phan-Quang, X. Han, M. R. Lee, Z. Yang, X. Y. Ling, *Angew. Chem. Int. Ed.* **2017**, *56*, 8813–8817; *Angew. Chem.* **2017**, *129*, 8939–8943.
[12] a) N. P. W. Pieczonka, R. F. Aroca, *ChemPhysChem* **2005**, *6*, 2473–2484; b) R. A. Álvarez-Puebla, *J. Phys. Chem. Lett.* **2012**, *3*, 857–866.
[13] M. Liebel, N. Pazos-Perez, N. F. van Hulst, R. A. Alvarez-Puebla, *Nat. Nanotechnol.* **2020**, *15*, 1005–1011.
[14] L. Saemisch, M. Liebel, N. F. van Hulst, *Nano Lett.* **2020**, *20*, 4537–4542.
[15] P. Mao, C. Liu, **2020**, *12*, 93–102.
[16] M. Blanco-Formoso, M. Turino, B. Rivas-Murias, L. Guerrini, A. Shavel, R. de la Rica, M. Correa-Duarte, V. Salgueiriño, N. Pazos-Perez, R. A. Alvarez-Puebla, *J. Phys. Chem. C* **2020**, *124*, 3270–3276.
[17] N. G. Bastús, F. Merkoçi, J. Piella, V. Puntes, *Chem. Mater.* **2014**, *26*, 2836–2846.
[18] B. Mir-Simon, I. Reche-Perez, L. Guerrini, N. Pazos-Perez, R. A. Alvarez-Puebla, *Chem. Mater.* **2015**, *27*, 950–958.
[19] a) H. K. Lee, Y. H. Lee, C. S. L. Koh, G. C. Phan-Quang, X. Han, C. L. Lay, H. Y. F. Sim, Y.-C. Kao, Q. An, X. Y. Ling, *Chem. Soc. Rev.* **2019**, *48*, 731–756; b) G. C. Phan-Quang, H. K. Lee, H. W. Teng, C. S. L. Koh, B. Q. Yim, E. K. M. Tan, W. L. Tok, I. Y. Phang, X. Y. Ling, *Angew. Chem. Int. Ed.* **2018**, *57*, 5792–5796; *Angew. Chem.* **2018**, *130*, 5894–5898.
[20] P. Nordlander, C. Oubre, E. Prodan, K. Li, M. I. Stockman, *Nano Lett.* **2004**, *4*, 899–903.
[21] C. Novo, A. M. Funston, I. Pastoriza-Santos, L. M. Liz-Marzán, P. Mulvaney, *Angew. Chem. Int. Ed.* **2007**, *46*, 3517–3520; *Angew. Chem.* **2007**, *119*, 3587–3590.
[22] a) M. Moskovits, J. S. Suh, *J. Phys. Chem.* **1984**, *88*, 1293–1298; b) M. Moskovits, J. S. Suh, *J. Phys. Chem.* **1984**, *88*, 5526–5530.
[23] L. Saemisch, M. Liebel, N. F. van Hulst, *Nanoscale* **2020**, *12*, 3723–3730.
[24] U. Ortiz-Orruño, A. Jo, H. Lee, N. F. van Hulst, M. Liebel, *Nano Lett.* **2021**, *21*, 317–322.

Manuscript received: January 3, 2022
Accepted manuscript online: February 2, 2022
Version of record online: March 16, 2022